

https://dspace.org/

# Transitional pressure drop in a cavitied microchannel

**Y Liu; Sjouke Schekman; Mo Xiao Li; Tian Jian Lu; T Kim**

https://hdl.handle.net/10539/42053
WOS

Downloaded from a DSpace repository. https://dspace.org/

# Transitional pressure drop in a cavitied microchannel

Yan Yan Liu [1,2] Sjouke W. Schekman [3] Mo Xiao Li [1,2]
Tian Jian Lu [1,2] and Tongbeum Kim [1,2,3,*]

[1]*MIIT Key Laboratory of Multifunctional Lightweight Materials and Structures, Nanjing University of Aeronautics and Astronautics, Nanjing 210016, People's Republic of China*
[2]*State Key Laboratory of Mechanics and Control for Aerospace Structures, Nanjing University of Aeronautics and Astronautics, Nanjing 210016, People's Republic of China*
[3]*School of Mechanical and Aeronautical Engineering, University of the Witwatersrand, Johannesburg 2000, South Africa*

(Received 26 July 2023; accepted 14 March 2024; published 5 April 2024)

Microchannels have become prevalent as an integrated part of microfluidic devices in biochemistry and electronics applications. In such devices, the small scale results in a characteristically low Reynolds number laminar flow. The small scale also results in an associated high flow resistance. A design concept has been developed that reduced the flow resistance by featuring geometrically modified microchannels with cavities. Compared to an unmodified microchannel, the modification reduces flow resistance at low Reynolds numbers but conversely leads to higher flow resistance at high Reynolds numbers: i.e., a reversal of flow resistance occurred. Thus far, plausible fluidic mechanisms underlying such reversal have remained largely unstipulated. Based upon detailed pressure and flow field measurements, we stipulate that flow progression from laminar flow slippage to rotational vortices in cavitied microchannels is the main mechanism causing the reversal. We further clarify that the earlier transition of initial laminar flow to turbulent flow is triggered by instabilities generated along shear layers, formed between the mainstream flow and rotational vortices in each cavity.

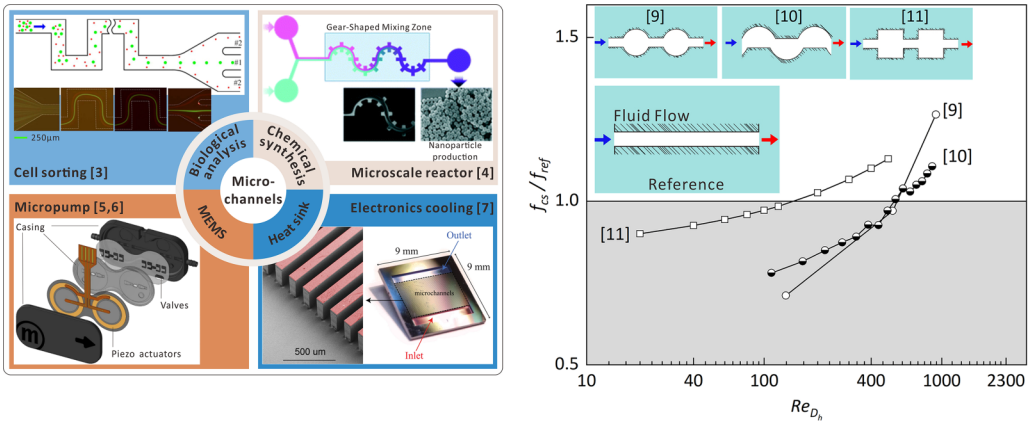
DOI: 10.1103/PhysRevFluids.9.044201

## I. INTRODUCTION

Microfluidic devices can process or manipulate small amounts of fluids [1] using multiple microchannels with hydraulic diameters typically ranging from tens to hundreds of micrometers. The compact design of microchannels offers advantages such as rapid and precise fluid control, high resolution and sensitivity, and large surface-area-to-volume ratios [1,2]. These features enable their widespread applications in various fields, as illustrated in Fig. 1(a) [3–7]. In these application scenarios, the fluid is usually pumped through the microchannels at a certain flowrate. This flow rate is such that the convective flow is largely laminar in the applications considered: the pressure drop is, therefore, primarily caused by friction between the forced flow and bounding surfaces. Further, for a given Reynolds number, the pressure drop per unit length ($\Delta P/L$) is substantially higher than that in macroscale channels, as a result of the small characteristic scale ($D$), e.g., $\Delta P/L \sim D^{-4}$ according to the Darcy-Weisbach equation [8]. Consequently, microchannels require a stronger pump for desired operations. The reduction of the flow resistance (i.e., pressure drop) across microchannels has thus become an important design consideration.

*Corresponding author: tongbeum.kim@nuaa.edu.cn

 ©2024 American Physical Society




(a) (b)

FIG. 1. Microfluidics: (a) Microchannels in micro-electro-mechanical systems (MEMS) in biomedical and electronics cooling applications [3–7] and (b) reversal of flow resistance quantified by friction factor ratios ($f_{CS}/f_{ref}$) for microchannels without and with cavitied sidewalls [9–11].

For thermal management of micro-electro-mechanical systems (MEMS), a microchannel design with wall modification is one of the noteworthy strategies that have been envisioned [9–12]. It is generally accepted that wall modification can enhance heat transfer at the expense of increased pressure drop [12]. One interesting work by Xia *et al.* [9] shows reduced flow resistance in a microchannel by introducing hemicircular cavities (termed "aligned fan-shaped" cavities) along its sidewalls as shown in the inset for Fig. 1(b). Their numerical results indicate that, at low Reynolds numbers, the flow resistance (in terms of the friction factor, $f$) for the cavitied microchannel is lower than the reference, unmodified microchannel [i.e., $f_{CS}/f_{ref} < 1.0$; Fig. 1(b)]. Increasing the Reynolds numbers increases the flow resistance and, at a certain Reynolds number, the flow resistance across the cavitied microchannel becomes characteristically larger than that of the reference microchannel, i.e., $f_{CS}/f_{ref} > 1.0$. In the current study, we term this feature as "the reversal of flow resistance." Subsequent numerical studies also observe such reversal by modifying the microchannel sidewalls with different cavity configurations, such as offset fan-shaped [10] and rectangular [11] cavities, as illustrated by the insets in Fig. 1(b).

The current consensus on plausible physical mechanisms responsible for the reversal of flow resistance is summarized as follows, based on [9–11]. At lower Reynolds numbers, the flow of fluid "slips" across the sidewall cavities. The cavity is considered to contain trapped and largely stagnant fluid. There is a much lower friction between the forced mainstream and cavity fluid compared to the friction between the mainstream and noncavitied sidewalls. The result is a decrease in flow resistance locally through the cavity. At higher Reynolds numbers, however, "jet" and "throttling" effects emerge. Such effects can cause exacerbated flow resistance. This explanation is seen as insufficiently precise. Specifically, no descriptive physical mechanisms have been stipulated hitherto. The predominant focus on numerical studies in those prior studies [9–11] further complicates this. These studies validate their numerical simulation results against pressure drop theory on reference, unmodified microchannels. The modeling of jet, throttling, and slipping effects are thus not strictly validated.

In the current study, we aim to squarely address the following specific issues:

(a) experimentally reveal the reversal of flow resistance in unmodified (reference) and modified microchannels by cavities, over a wide range of laminar Reynolds numbers;

(b) stipulate a fluidic loss mechanism, i.e., the so-called "flow slippage," at relatively low laminar Reynolds numbers; and

TABLE I. Geometric parameters of the three tested circular microchannels.

| | $L_0$ (mm) | $l_0$ (mm) | $D_0$ (mm) | $D_1$ (mm) | $L'_0$ (mm) |
|---|---|---|---|---|---|
| Reference (ref) microchannel | 50 | 2.5 | 0.5 | 2.0 | / |
| Two/three-dimensional cavitied sidewall (CS) microchannels | | | | | $1.27L_0$ |

(c) stipulate a fluidic loss mechanism, i.e., the so-called "jetting and throttling effects," at relatively high laminar Reynolds numbers.

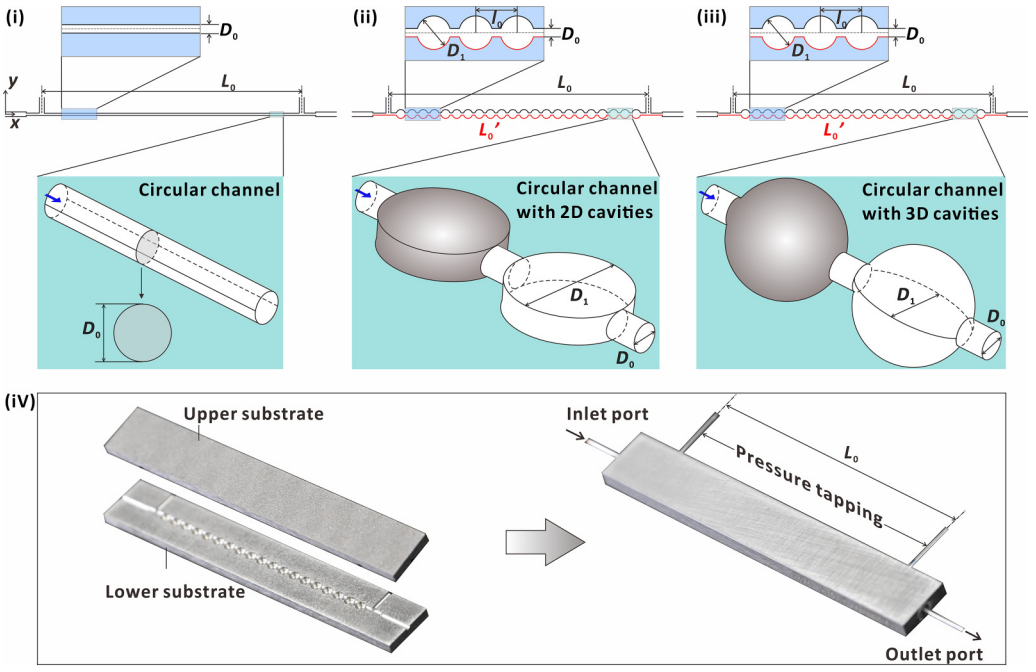
To this end a series of microchannels with hydraulic diameters of $115.5\,\mu\text{m} \leqslant D_h \leqslant 500\,\mu\text{m}$ are studied at $\text{Re}_{D_h} = 50 - 1180$. This includes both reference (unmodified) channels and channels with hemicircular cavities. Further, both two-dimensional (2D; e.g., a disk) and three-dimensional (3D; e.g., a sphere) cavities have been considered. In this way, the stipulated mechanisms can be assessed further. For example, a flow slippage mechanism might be enhanced by the removal of all sidewalls in a 3D cavity, compared to just half the sidewalls in a 2D cavity. To the best of the authors' knowledge, only 2D cavities have been considered hitherto. It is worth noting that the comparison in previous studies is between unmodified and cavitied microchannels. To stipulate the fluidic mechanism of reversal flow resistance, a comparison between unmodified and cavitied microchannels is also followed in our study. To demonstrate detailed flow patterns, microparticle image velocimetry ($\mu$PIV) is utilized, necessitating a transparent microchannel.

## II. EXPERIMENTAL DETAILS

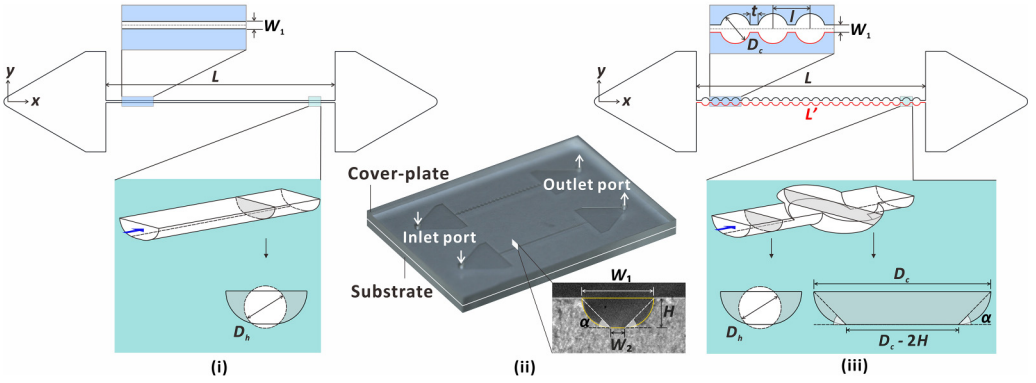
### A. Microchannel specimens and test setup

Three metallic circular microchannels are fabricated [Fig. 2(a)], including a reference (unmodified) microchannel and two other sets of microchannels respectively modified by 2D and 3D cavities. The designed micropassage is machined by Micro-Computer Numerical Control (Micro-CNC) on 1.5-mm-thick stainless-steel upper and lower substrates. After machining, the two substrates are rebonded by diffusion welding. The cross section of the reference microchannel is circular with its inner diameter of $D_0 = 500\,\mu\text{m}$. At 2.0 mm downstream from the entrance and 2.0 mm upstream from the exit of the test section, two static pressure tapping holes in 0.5 mm diameter are machined with a 50-mm center-to-center distance. As for the cavitied circular microchannels, 19 pairs of 2D and 3D cavities with a diameter of $D_1 = 2.0$ mm, are aligned along the straight micropassage, with the center-to-center spacing fixed at $l_0 = 2.5$ mm (Table I).

To explore the flow field inside the unmodified and cavitied microchannels using $\mu$PIV, two transparent microchannel specimens, reference and modified with 2D cavities, are additionally fabricated, as shown in Fig. 2(b). The Micro-CNC process would have resulted in nontransparent surfaces, which is not appropriate. For both specimens, a designed micropassage is chemically etched out by hydrogen fluoride on a 2.0-mm-thick transparent quartz glass substrate, and a 2.0-mm-thick cover plate is press-fused on top of the substrate [Fig. 2(b)]. This results in a rectangular cross-section shape with round bottom corners, as shown in the inset of Fig. 2(b). Upstream of and downstream frrom each micropassage, a wide-angle diffuser-type chamber is added to uniformly distribute a supplied working fluid—deionized (DI) water—into the test passage. Geometrical dimensions of the reference microchannel are $W_1 = 200\,\mu\text{m}$ (top base), $W_2 = 20\,\mu\text{m}$ (bottom base), $H = 90\,\mu\text{m}$ (height), $\alpha = 45^\circ$ (taper between the top and bottom bases), and $L = 22.81$ mm (total length), as indicated in Fig. 2(b). As for the cavitied microchannel, 22 pairs of cavities with top diameter $D_c = 0.8$ mm, are aligned along the straight micropassage, with the center-to-center spacing fixed at $l = 1.0$ mm (Table II).




(a)




(b)

FIG. 2. Microchannel specimens: (a) Circular microchannels include (i) a reference circular microchannel, (ii) a 2D cavitied circular microchannel, (iii) a 3D cavitied circular microchannel, and (iv) photographs of a fabricated microchannel showing upper and lower substrates, and designed micropassage. (b) Rectangular microchannels include (i) a reference rectangular microchannel, (ii) a photograph of a fabricated microchannel showing cover plate, substrate, and designed micropassage, and (iii) a 2D cavitied rectangular microchannel.

The prepared microchannel specimens are set up for flow resistance and flow field measurements. DI water as a working fluid is supplied using a syringe pump (Harvard Apparatus) via an inlet port drilled on the cover plate and drained through an outlet port. Prior to experimental measurements, the syringe pump is calibrated in the range of 0.100–20.000 ml/min by measuring the mass of pumped DI water at the outlet port using an analytical balance (BSA124S, Sartorius).

TABLE II. Geometric parameters of the two tested rectangular microchannels.

| | Cross section | | | | | | | | | |
|---|---|---|---|---|---|---|---|---|---|---|
| | $W_1$ (μm) | $W_2$ (μm) | $H$ (μm) | $\alpha$ (deg) | $L$ (mm) | $D_h$ (μm) | $L'$ (mm) | $l$ (mm) | $t$ (mm) | $D_c$ (mm) |
| Reference (ref) microchannel | 200 | 20 | 90 | 45 | 22.81 | 115.5 | / | / | / | / |
| Two-dimensional cavitied sidewall (CS) microchannel | | | | | | | 1.27$L$ | 1.0 | 0.23 | 0.8 |

### B. Time-averaged static pressure measurements

The experimental setup for measuring time-averaged flow resistance (or pressure drop) is detailed in Fig. 3. A differential pressure transducer (PX409, Omega Engineering) is connected to the inlet and outlet ports of the microchannel, monitoring a pressure difference as DI water flows at differing flow rates. The output signal of the differential pressure transducer is recorded by a data acquisition system (34972A, Keysight Technologies) at 20 Hz for 60 s, collecting 1200 sampled signals. The voltage signals are then converted and time averaged to obtain the mean pressured drop for a given flow rate.

### C. Time-averaged flow field measurements using microparticle image velocimetry

The local flow field inside the microchannel with the cavitied sidewall is mapped by a $\mu$PIV system, as schematically shown in Fig. 3. Detailed descriptions of the $\mu$PIV system and experimental setup are provided in Supplemental Material I [13] (see also [14–17]).

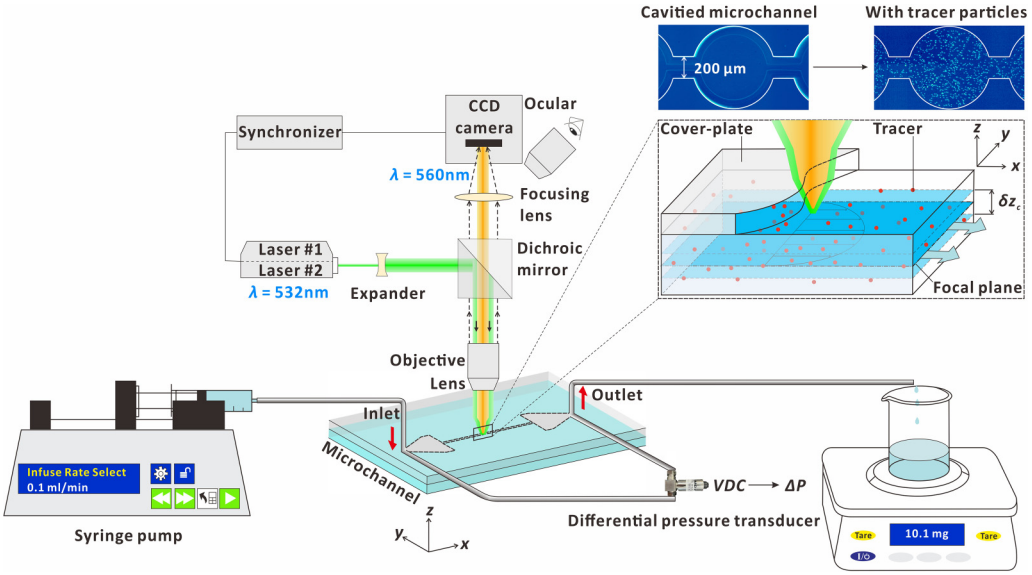



FIG. 3. Experimental setup for measuring pressure drop and local flow fields using a $\mu$PIV system.

### D. Data reduction parameters and measurement uncertainties

Throughout the present study, the Reynolds number ranges from $50 \leqslant \mathrm{Re}_{D_h} \leqslant 1180$. For circular microchannels shown in Fig. 2(a), the hydraulic diameter is equal to its diameter, e.g., $D_h = D_0$. For noncircular microchannels specific to the present configurations [Fig. 2(b)], the hydraulic diameter is defined as

$$D_h = \frac{4A_c}{P} = \frac{4[HW_2 + (\pi H^2)/2]}{W_1 + W_2 + \pi H}, \tag{1}$$

where $H$, $W_1$, and $W_2$ denote the micropassage height and the width of the top and bottom bases, respectively [Fig. 2(b) and Table II]. This is the same convention adopted by previous microchannel investigations [9–11] but does not consider the varying cross-sectional area of the channel due to cavity modifications. Nonetheless, upon comparing the reference and cavitied channels [Figs. 2(a) and 2b)], however, Eq. (2) can be seen as being more suitable. If the variation in the cross-sectional area was considered, the adjusted hydraulic diameter ($D_h'$) would be $1.23D_h$ where $D_h' = 4V/S$, $V$ is the fluid volume, and $S$ is the channel surface area. Based on the hydraulic diameter ($D_h$) of the reference microchannel, $\mathrm{Re}_{D_h}$ is defined as

$$\mathrm{Re}_{D_h} = \frac{\rho u_m D_h}{\mu}, \tag{2}$$

where $\rho$ and $\mu$ are separately the density and dynamic viscosity of DI water, and $u_m$ is the mean velocity (setting value with the precalibrated syringe pump). The density and dynamic viscosities of DI water at local temperature (20 °C) and barometric pressure (100 kPa) are 998.21 kg/m$^3$ and $1.0016 \times 10^{-3}$ Pa s, respectively.

As a nondimensional measure of flow resistance, the friction factor is calculated as

$$f_{D_h} = \left(\frac{2\Delta P}{L}\right)\left(\frac{1}{\rho u_m^2}\right)D_h, \tag{3}$$

where $\Delta p$ is the pressure drop between the inlet and outlet ports of the specimen measured by a differential pressure transducer, and $L$ is the straight length of the micropassage.

The uncertainty of mean velocity is associated with flow rate and cross-sectional area and is estimated to be 0.62%. Similarly, the estimated uncertainties of Reynolds number and pressure drop per unit length are within 0.86% and 1.00%, respectively. The uncertainty of the friction factor that is associated with the mean velocity, hydraulic diameter, and pressure drop per unit length, is estimated to be less than 1.81%. Uncertainty of the instantaneous velocities measured by $\mu$PIV is estimated to be 3.73%. Detailed calculation of uncertainties for all the parameters is provided in Supplemental Material II [18] (see also [19–23]).

## III. DISCUSSION OF RESULTS

### A. Overall flow resistance (pressure drop)

The dependence of flow resistance on mean velocity is firstly quantified by pressure drop per unit length ($\Delta p/L$) in microchannel specimens. The results for the unmodified (reference), 2D, and 3D cavitied circular channels are compared in Fig. 4(a). The mean velocity varies from 0.09 m/s up to 1.9 m/s. This corresponds to the Reynolds number range of $\mathrm{Re}_{D_h} = 100 - 930$, which implies laminar flow in the three circular microchannels. The entry length ($L_{\mathrm{entry}}$) formed by developing laminar flow varies with the Reynolds number typically as $L_{\mathrm{entry}} = 0.06D_h\mathrm{Re}_{D_h}$ with $6D_h \leqslant L_{\mathrm{entry}} \leqslant 55.8D_h$ in the present setup. Given that the total channel length is $L_0 = 100D_h$, the contribution of the entry region to the total pressure drop might be negligible at low $\mathrm{Re}_{D_h}$ but becomes substantial at high $\mathrm{Re}_{D_h}$.

Laminar flow in the reference circular channel causes the flow resistance (in terms of $\Delta p/L$) to increase almost linearly in the tested mean velocity range. With the 2D cavities, the pressure drop

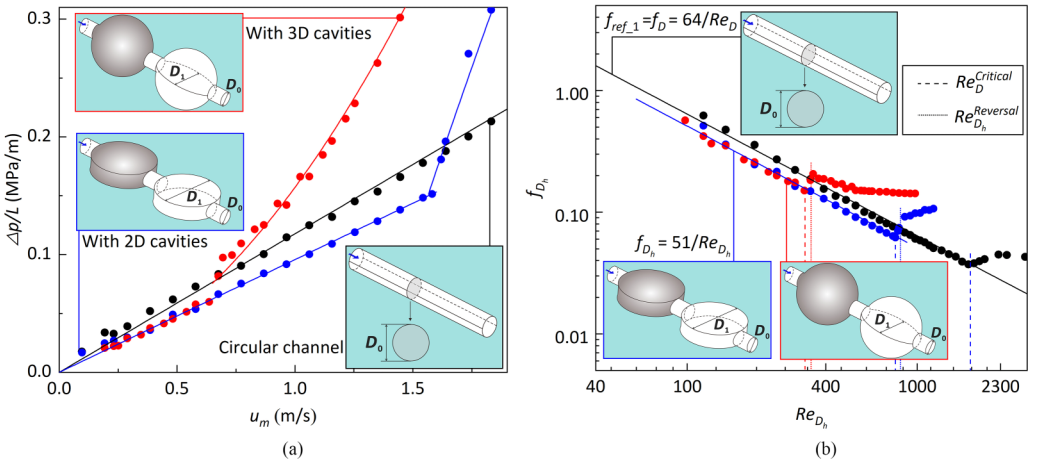



FIG. 4. Comparisons between unmodified (reference) and cavitied circular microchannels for (a) pressure drop per unit length and (b) friction factor.

is observed to be lower than the reference microchannel. It consistently increases linearly with the mean velocity until $u_m \sim 1.6$ m/s, after which its increasing trend deviates from the linear increase, becoming steeper. At $u_m = \sim 1.64$ m/s, an equivalent flow resistance between the reference and 2D cavitied circular microchannels is measured. With a further increase in $u_m$, the flow resistance in the 2D cavitied microchannel becomes higher than that in the reference one—the reversal of flow resistance.

Considering the microchannel with 3D cavities, the flow resistance initially follows the microchannel with 2D cavities as shown in Fig. 4(a). Both 2D and 3D cavitied microchannels exhibit a linear and lower flow resistance than the reference microchannel. However, like the 2D cavitied microchannel, there is a sudden deviation from the linear increase. The onset mean velocity value is, however, much lower: $u_m = 0.63$ m/s for the 3D cavities vs $u_m = 1.6$ m/s for the 2D cavities. With a further increase in the mean velocity, e.g., $u_m = 0.67$ m/s, the flow resistance becomes equivalent to the reference case followed by a higher-pressure drop occurring from the 3D cavitied microchannel—the reversal of flow resistance.

In summary, the pressure drop in microchannels with either 2D or 3D cavities is reduced in contrast to the reference microchannel at low mean velocities (e.g., 25% lower at $u_m = 0.5$ m/s). The pressure drop in both cavitied microchannels is identical in magnitude. However, the onset mean velocity that causes the deviation from the linear increase substantially differed—an earlier deviation with 3D cavities. Immediately after the deviation, the pressure drop in the cavitied microchannels is reversed to be higher than the reference (unmodified) microchannel. A similar reversal of flow resistance is also observed between the unmodified (reference) and cavitied (with 2D cavities) rectangular microchannels [Fig. 5(a)]. The equivalent pressure drop between the two microchannels is obtained at $u_m = \sim 6.58$ m/s. Prior to this mean velocity ($u_m = \sim 6.58$ m/s), the 2D cavitied microchannel has a lower pressure drop than the reference one (e.g., 26% lower at $u_m = 3.0$ m/s).

To comprehend the dependence of flow resistance across a given channel on mean velocity, the pressure drop per unit length ($\Delta p/L$) is generalized using a friction factor, $f_{Dh}$ (or $f_D$). As a reference, the friction factor of the microchannel with a circular cross section (hydraulic diameter, $D_h$) for laminar flow is plotted in Fig. 4(b). Our data points for the reference microchannel fit well with the established theory: $f_{\text{ref_1}} = f_D = 64/\text{Re}_D$ [4]. In comparison, the friction factor of the 2D and 3D cavitied microchannels at lower Reynolds numbers, are empirically correlated as $f_{Dh} = 51/\text{Re}_{D_h}$, indicating the linear dependence, i.e., $\Delta p/L \sim u_m$ and yet 20% lower friction factors.

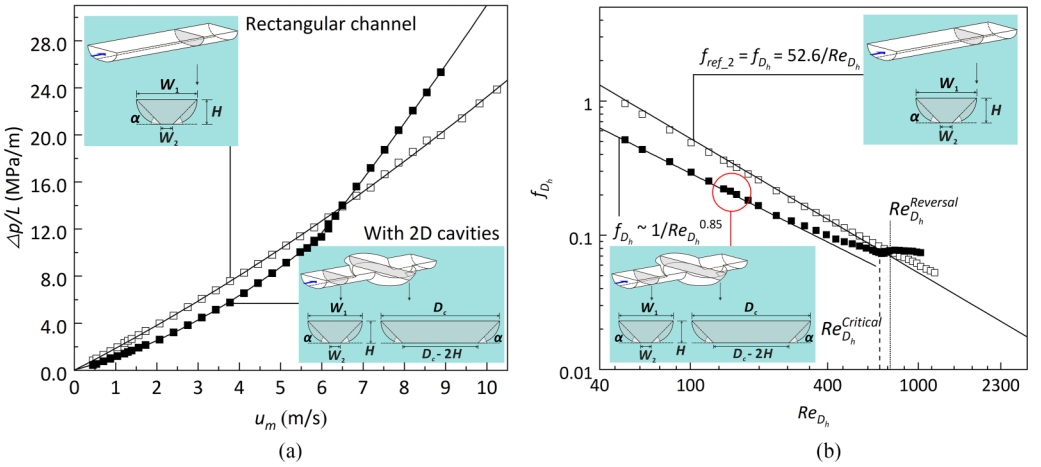



FIG. 5. Comparisons between an unmodified (reference) and a circular cavitied microchannel with a rectangular cross section featuring curved sidewalls for (a) pressure drop per unit length and (b) friction factor.

For the reference circular microchannel, the transition to turbulent flow appears to take place at $\mathrm{Re}_{D_h} \sim 1700$, as indicated by the sudden deviation (increase) in friction factor [Fig. 4(b)]. This Reynolds number is roughly consistent with the widely accepted critical Reynolds number of 2000–2300. With circular cavities, there also exists a sudden deviation (increase) in friction factor. These deviations, however, occur at a lower Reynolds number of $\mathrm{Re}_{D_h} = 803$ and 323 for the 2D and 3D cavitied circular microchannels, respectively. At $\mathrm{Re}_{D_h} \sim 845$ and 345, the magnitude of the friction factors (for 2D and 3D cavities, respectively) exceeds the reference microchannel—the reversal of flow resistance. We term these here as the "reversal" Reynolds number. From the point of deviation, the variation of friction factor for microchannels with cavities is similar to that for the reference microchannel. There are, however, differences. For example, the deviation is more rapid with cavities (both 2D and 3D) and the 3D cavitied microchannel friction factor almost immediately begins decreasing after the sudden deviation. A further increase in the Reynolds number may lead to the insensitive variation of the friction factor to the Reynolds numbers by configuring a plateau—the scaling of $\Delta p/L \sim (u_m)^2$. Despite the small differences, all deviations are considered as transitions from laminar to turbulent flow. The occurrence of the significantly earlier transition to turbulent flow has also been consistently observed in other 2D cavitied microchannel studies [24,25]. Our results in Fig. 4(b) further indicate that the 3D cavities cause a much earlier transition than that caused by the 2D cavities. However, before the transition, the flow resistance in magnitude is identical. This indicates that when the flow slippage mechanism is in effect and preceding the reversal of flow resistance, there is no benefit or detriment to the use of 3D over 2D cavities.

The variation of flow resistance with Reynolds number has been shown for both 2D and 3D cavitied microchannels. The fluidic mechanisms responsible for such variations are still, however, unclear. To investigate these, a set of transparent microchannels is used, allowing for $\mu$PIV measurements. The variation of pressure drop per unit length and friction factor for these channels are shown in Fig. 5. The reference (unmodified) microchannel cross section may be simplified into an isosceles trapezoidal cross section [based on Fig. 2(a)(iii)] as to follow $f_{\mathrm{ref_2}} = f_{Dh} = 52.6/\mathrm{Re}_{D_h}$ [26]. Our experimental data agree well with the simplified estimate ($f_{\mathrm{ref_2}}$) as seen in Fig. 5(b). With the (2D) cavities, the dependence of pressure drop on the mean velocity slightly differs from the classical theory, i.e., $\Delta p/L \sim (u_m)^{1.15}$ instead of $\Delta p/L \sim (u_m)^{1.0}$ [Fig. 5(a)]. This implies that the flow resistance scales with the Reynolds number nonlinearly—the flow resistance acquires a slightly higher gradient at larger, yet still laminar, Reynolds numbers. Regarding Fig. 5(b), it can be seen that the critical Reynolds number (where sudden deviation in friction factor occurs) and the reversal

Reynolds numbers (where the friction factor of the reference and cavitied channels are equal) are 720 and 758, respectively. Both values are higher than those for the circular microchannels with the 2D and 3D cavities [Fig. 4(b)].

In summary, it is common that regardless of the microchannel cross-section shape, the cavities function to reduce flow resistance ∼25% lower over the respective reference microchannels. An earlier transition to turbulent flow is triggered by the cavities while the 3D cavities incite an even earlier transition than the 2D cavities. Yet, until the transition, the reduction of flow resistance in comparison to the reference microchannels is identical. The transition precedes the reversal of flow resistance and higher-pressure drop from the cavitied microchannels than the reference microchannels.

### B. Flow pattern inside 2D sidewall cavity

To reveal the mechanism that possibly caused the reversal of flow resistance, we define a new parameter that quantifies the difference in pressure drop per unit length between the two transparent microchannels with a rectangular cross section, as

$$\Delta = \left(\frac{\Delta p}{L}\right)_{\text{ref}} - \left(\frac{\Delta p}{L}\right)_{\text{CS}}, \tag{4}$$

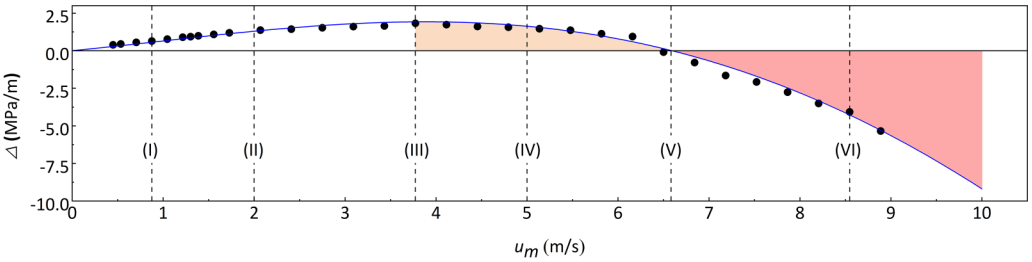
where the subscripts "ref" and "CS" denote the reference and cavitied sidewalls, respectively. A positive value (i.e., $\Delta>0$) means a higher pressure drop from the reference microchannel than the 2D cavitied microchannel, while a negative value indicates the opposite. The results of Fig. 6(a) depict an increase in $\Delta$ until $u_m = 3.8$ m/s ($\text{Re}_{D_h} = 438$) where it peaks. Then, a further increase in $u_m$ leads to a decrease in $\Delta$ until $u_m = 6.58$ m/s ($\text{Re}_{D_h} = 758$) but still $\Delta > 0$. After the reversal that occurs at $u_m = 6.58$ m/s, $\Delta$ becomes negative, with a steep decrease as $u_m$ is further increased.

To understand the fluidic cause responsible for each dependence on mean flow velocity, the flow field within a sidewall cavity situated at the midlength of the rectangular microchannel is examined in detail. The nominal distance from the channel inlet to the selected cavity cell indicates that the mainstream is fully developed within the entire Reynolds number range considered. Six representative mean velocities, case I at $u_m = 0.88$ m/s, case II at 2.00 m/s, case III at 3.80 m/s, case IV at 5.00 m/s, case V at 6.58 m/s, and case VI at 8.55 m/s, are selected, as denoted in Fig. 6(a).

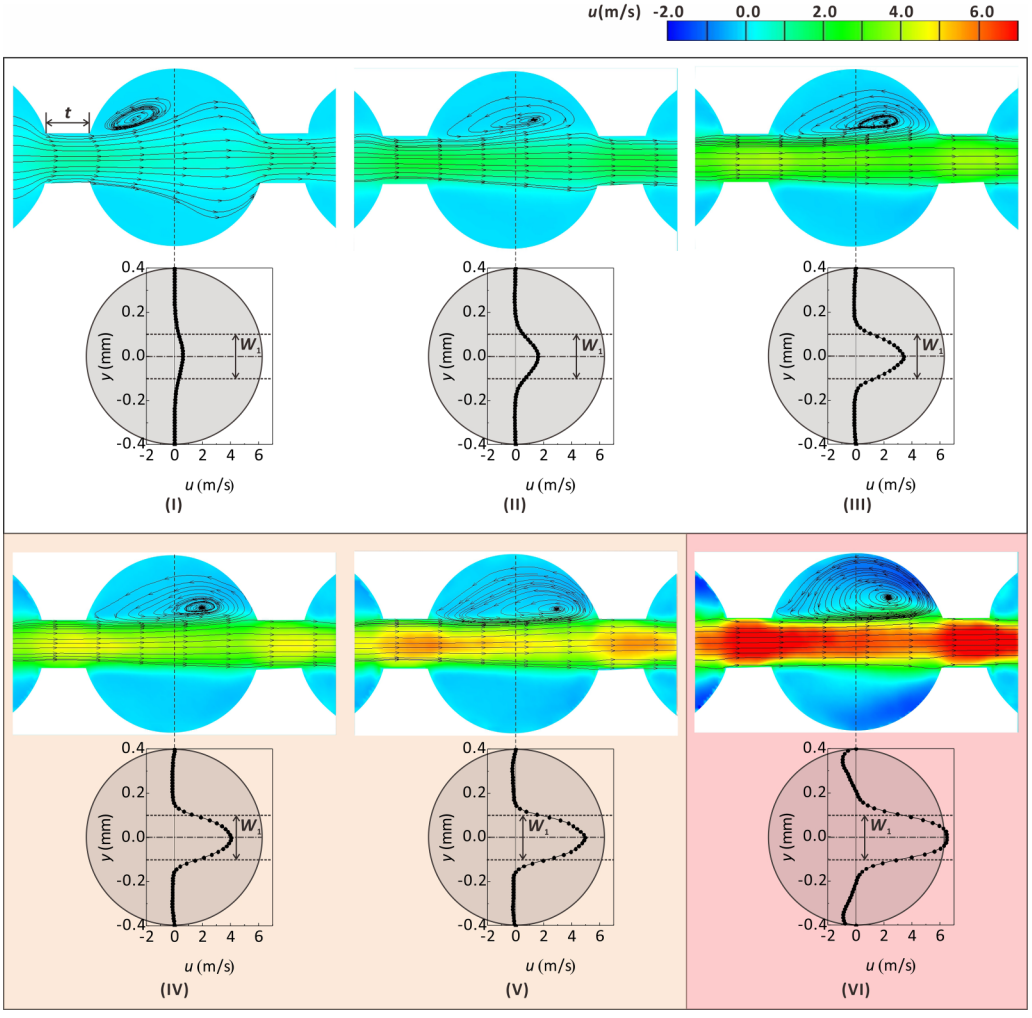
Case I denotes a very low momentum fluid entering the sidewall cavity through an orificelike straight throat ($t/D_h = 2.0$), where $t$ is the throat length and $D_h$ is the hydraulic diameter of the throat. The streamlines that immediately separate from the sharp lid of the throat inlet form a stream tube. This can be seen by (I) in Fig. 6(b) using the axial velocity component ($u$) contour based on our $\mu$PIV data. The outermost separated streamlines of the stream tube roll up to form a small vortex that resides near the throat exit. The momentum is very weak, and the fluid flow diffuses radially as it moves downstream from the cavity inlet (or throat exit). Due to the relatively high static pressure at the inlet of the successive throat by contraction, the stream tube inflates radially immediately upstream of the throat inlet. The radial profile of $u$ is extracted from the velocity contours along the central cavity plane perpendicular to the channel axis. The radial profile indicates that the fluid within the cavity, especially near the cavity wall, is nearly stagnant (i.e., $u \sim 0.0$ m/s at $y = \pm 0.4$ mm).

As the mean velocity increases (cases II and III), the increased momentum of fluid causes an enlarged vortex whose core is pushed farther downstream away from the cavity inlet. The coverage of the vortex within the sidewall cavity becomes larger as well. However, for both cases, the radial profiles of $u$ show no sign of fluid motion along the cavity walls. In addition, the extent of the previously observed radial inflation of the stream tube near the throat inlet becomes reduced. The streamlines display a more straightened flow path for each stream tube.

As the mean velocity continues to increase (cases IV and V), the vortex can be seen to be further enlarged within the sidewall cavity but still does not fill the entire cavity. The streamlines are




(a)




(b)

FIG. 6. Flow resistance and flow field varying with mean flow velocity ($u_m$): (a) pressure drop difference ($\Delta$) and (b) flow structure and velocity profile within a representative cavity cell measured with a $\mu$PIV system.

straightened further. One noticeable feature can be seen: the fluid in the vicinity of the concave sidewalls ($\sim y = \pm 0.4$ mm) begins to move in the opposite direction to the mainstream—the emergence of a weak reverse flow.

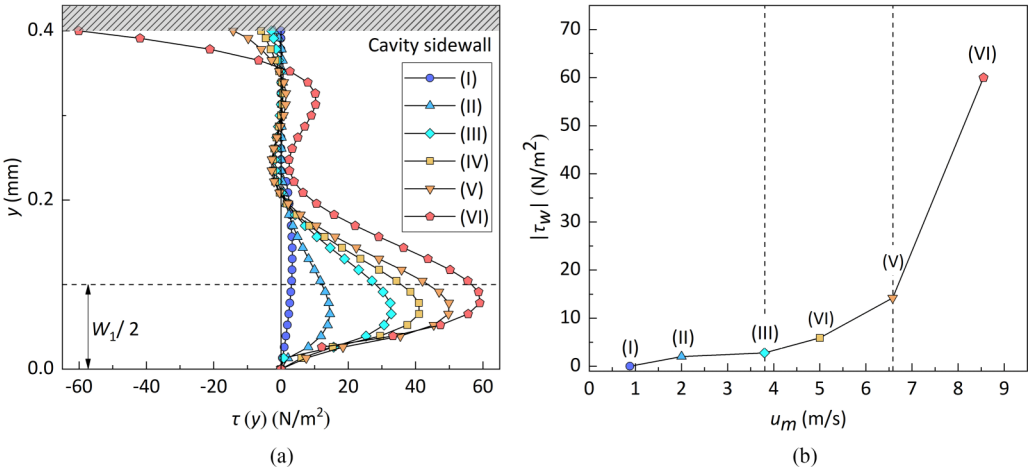



FIG. 7. Shear stress ($\tau$) distribution at six selected $u_m$ values: (I) at $u_m = 0.88$ m/s, (II) at 2.00 m/s, (III) at 3.80 m/s, (IV) at 5.00 m/s, (V) at 6.58 m/s, and (VI) at 8.55 m/s. (a) In the fluid along the central cavity plane perpendicular to the nominal channel axis and (b) wall shear stress ($|\tau_w|$).

For case VI, after the reversal of flow resistance [Fig. 6(a)], the vortex formed by the separated streamlines occupies the entire sidewall cavity. Now, a strong reverse flow is present in the vicinity of the concave cavity wall ($\sim y = \pm 0.4$ mm), moving in the opposite direction to the mainstream. This strong reverse flow could generate apparent wall shear stresses along the concave cavity sidewall. As a result, the flow resistance is enlarged, possibly exceeding that of the reference microchannel. For a 3D cavity, there would be a larger surface area over which the reverse flow is acting and an increased flow resistance. This is taken to explain why, following the reversal Reynolds number, the 3D cavitied microchannel friction factor is higher than the 2D cavitied one in Fig. 4(b).

### C. Shear in the fluid inside 2D sidewall cavity

With laminar flow, the flow resistance is predominantly caused by friction between the moving fluid and solid surfaces. Following Newton's formula for the shear stresses given by

$$\tau(y) = \mu\left(\frac{du}{dy}\right), \tag{5}$$

the radial distribution of shear stresses in convective flow along the cavity's central plane is calculated. The results in Fig. 7(a) show that zero shears exist at the channel axis ($y = 0$), since $du/dy = 0$. The shear stress steeply increases towards the dividing streamlines that roughly coincide with the cavity interface ($y = \pm W_1/2$). Further, towards the cavity sidewall surface, it decreases substantially, being nearly zero at $y = R_c$ ($= \pm 0.4$ mm) for cases I–III. The stagnant fluid trapped in sidewall cavities acts as a buffer layer between the mainstream and concave cavity sidewalls, thus reducing friction between the mainstream and sidewall surfaces. This fluidic mechanism has previously been termed flow slippage, and now becomes stipulated. Interestingly, the expanding buffer layer's surface area between the mainstream and concave sidewalls, such as between 2D and 3D cavities, does not noticeably affect the friction factor as shown in Fig. 4(b).

For cases IV and V with higher mean mainstream velocities, the overall radial profile of shear stresses remains unchanged qualitatively. However, the magnitude of the peak shear stress located roughly at the cavity interface increases. Additionally, the wall shear stresses on the concave cavity surface at $y = R_c$ ($= \pm 0.4$ mm) become noticeable [Fig. 7(a)]. Now, the weak reverse flow in (IV) and (V) of Fig. 6(b) causes nonzero wall shear stresses. Thus, the flow resistance from sidewall cavities begins to be important, reducing the pressure drop difference ($\Delta$) as observed in Fig. 6(a).

The continuously increasing shear stresses along the concave cavity wall with increasing mean flow velocity eventually lead to the reversal of flow resistance (as noted in Figs. 4 and 5).

A further increase in mean velocity (i.e., $u_m > 6.58$ m/s, from case V to case VI) leads to the cavitied microchannel having a higher pressure drop than the reference microchannel [Fig. 6(a)]. This reversal of flow resistance seems to result from the strengthened wall shear stresses [Fig. 7(a)] by the enlarged vortex acting on the 27% elongated flow path (i.e., $L' = 1.27L$ along the concave cavity wall surface, as indicated in Fig. 2 and Table I), compared to the reference microchannel. Here, large flow circulation in the sidewall cavity is the main feature.

Figure 7(b) summarizes shear stresses calculated at $y = R_c$ ($= \pm 0.4$ mm). There is a marginal variation of wall shear stress ($|\tau_w|$) for cases I–III, as a negligible flow that is reversed within the sidewall cavity is driven by the mainstream. A noticeable increase in $|\tau_w|$ occurs from case III to case V, followed by a steep increase in case VI, which contributes to the reversal of flow resistance. However, the shear stress data discussed in Fig. 7 is a consequence of some fluidic features that have hitherto not been stipulated. We believe that the rotationality of fluid particles circulating within each sidewall cavity cell plays in part, if not in full, a certain role in strengthening the wall shear stresses. Thus, the vorticity field of the flow calculated based on our $\mu$PIV data is considered next.

### D. Vorticity inside 2D sidewall cavity

The increasing wall shear stresses along concave sidewall cavity surfaces, brought on by the increased Reynolds number, are the main cause of the observed "reversal of flow resistance." This reversal predominantly takes place after case V at $u_m = 6.58$ m/s in the present study. However, thus far it remains uncertain how and why the vortex formed in sidewall cavity yields (i) a substantial increase in wall shear stresses along concave cavity wall surfaces above the reversal Reynolds number ($\mathrm{Re}_{D_h} = 758$), triggering the reversal, and (ii) earlier transition of laminar to turbulent after the critical Reynolds number ($\mathrm{Re}_{D_h} = 720$). To this end, we consider fluid motion within sidewall cavities for six selected cases, focusing upon rotationality that is characterized by "vorticity ($w_z$)" as

$$w_z = \frac{dv}{dx} - \frac{du}{dy}. \tag{6}$$

Upon considering the upper half of the cavity and the fluid entering the throat of each cavity ($t/D_h = 2.0$) for case I, the fluid particles inside the redeveloping boundary layer at the throat inlet rotate in counterclockwise (CCW) direction. Such phenomena can be visualized in Fig. 8(I). In exiting the throat, a vortex is formed resulting from the sudden expansion of boundary layer flow into the sidewall cavity. However, due to the low momentum of the mainstream, the vorticity within the boundary layer is low and the vortex is small. Further, the rotational fluid particles seem to become irrotational as they convect over the cavity interface (i.e., $y \sim W_1/2$). This can be attributed to viscous damping by the fluid that fills the cavity. However, immediately after entering the throat, its rotationality is regenerated. Proceeding to case III via case II, the vorticity of the boundary layer flow in the throat is strengthened, as illustrated in Figs. 8(II) and 8(III). While a larger portion of the boundary layer flow over the cavity interface has rotational particles, the fluid in the cavity remains largely stagnant. The flow structures of cases I–III represent low Reynolds number conditions, below the reversal Reynolds number ($\mathrm{Re}_{D_h} \leqslant 758$), leading up to where $\Delta$ is maximized in case III [as per Fig. 6(a)]. Case I, as a representative, is schematically summarized in Fig. 9(a).

From case IV to case V, the increased mean velocity generates substantial vorticity in the boundary layer flow with its progressive strengthening, as shown in Figs. 8(IV) and 8(V). The rotational fluid particles induce the generation of shear layer instabilities along the cavity interface. Further, the vortex formed in the cavity becomes enlarged, yet fluid particles are still irrotational. Although weak, there exist signs of vorticity generation along concave sidewalls for case V, having a rotation in the opposite direction to boundary layer flow due to wall shear. Case IV represents the approach to the reversal Reynolds number (case V), as schematically represented in Fig. 9(b).

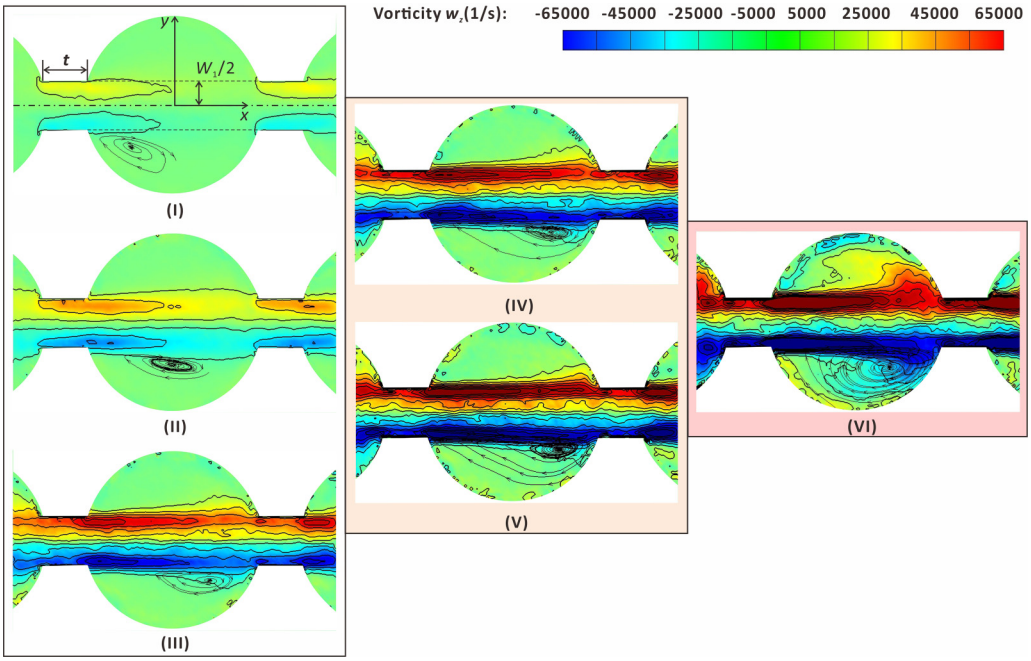



FIG. 8. Vorticity distribution inside the sidewall cavities at six selected Reynolds numbers where positive vorticity denotes a counterclockwise rotation: (I) $\mathrm{Re}_{D_h} = 100$, (II) $\mathrm{Re}_{D_h} = 230$, (III) $\mathrm{Re}_{D_h} = 438$, (IV) $\mathrm{Re}_{D_h} = 576$, (V) $\mathrm{Re}_{D_h} = 758$, and (VI) $\mathrm{Re}_{D_h} = 1000$.

In sharp contrast, for case VI, the separated streamlines enter the cavity with strong rotationality, as clearly visible in Fig. 8(VI). For the upper cavity, fluid particles within the central region of the cavity rotate in the CCW direction. The opposite holds for the lower cavity. Upon recalling case VI in Fig. 6(b), the strong reverse flow inside the cavity forms a boundary layer, which develops from concave cavity surfaces. Thus, vorticity in the opposite direction to that of the mainstream—clockwise (CW) direction—is generated. Case VI represents a state above the reversal Reynolds number and is schematically illustrated in Fig. 9(c). The primary characteristic of the flow pattern is the circulation of fluid particles accompanied by self-rotational motion, referred to as the "rotational vortices." In due course, the wall shear stresses become substantial, resulting in high flow resistance (higher than that of the reference microchannel), i.e., the reversal of flow resistance. We believe that previous studies [9–11] misleadingly term this collective feature as the "jetting and throttling effects." Instead, we have now stipulated that vortex kinematics in sidewall cavities is the main cause behind this feature.

In addition, the high vorticity flow forming the large rotational vortex inside the cavity disturbs the shear layers when the vortex recirculates and meets the shear layers. This, in turn, further increases the instabilities of shear layers along the cavity interface. Further, unstable shear layers trigger the earlier transition of laminar to turbulent flow—conjectured previously by the plateaulike feature in friction factor [Fig. 4(b)]. Moreover, the switch from 2D to 3D cavities then can be seen as increasing the surface area of the cavity on which the vortical flows act. In doing so, the overall wall shear stresses in the cavity would increase more rapidly, with increasing Reynolds number. Additionally, an earlier reversal of flow resistance could be expected, as is then confirmed in Fig. 4(b).

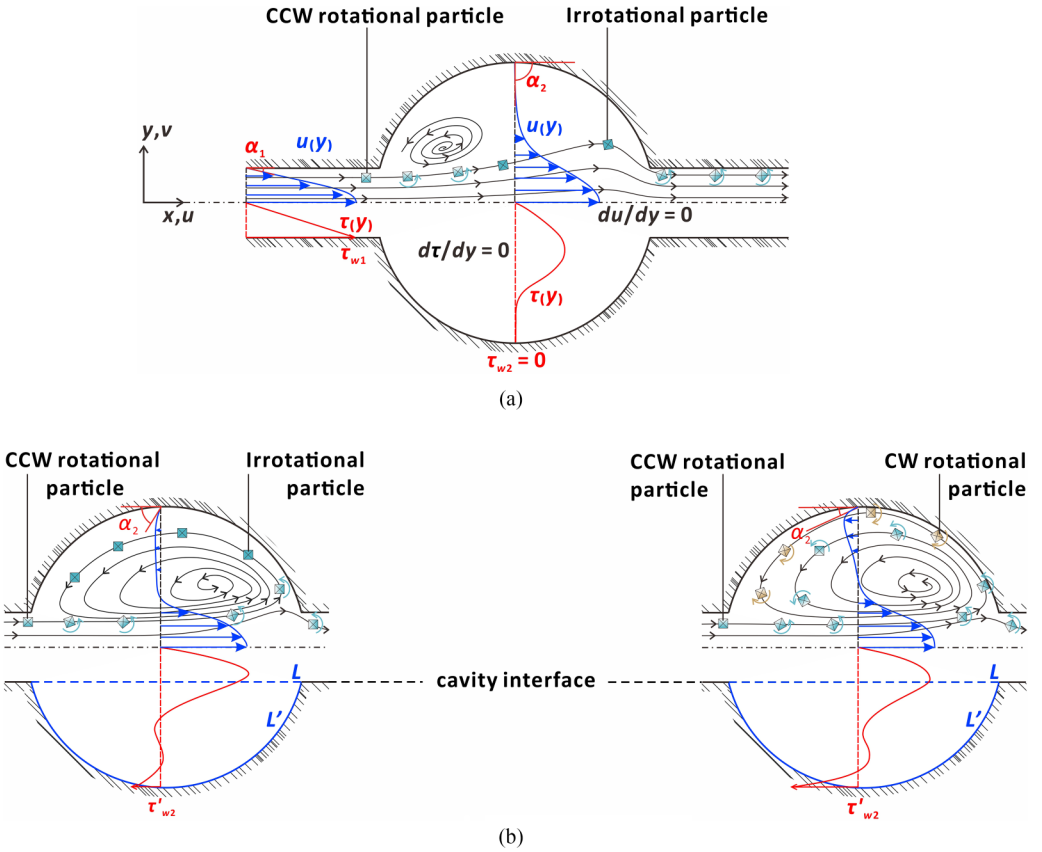



FIG. 9. Schematics of flow structure (in the $x$-$y$ plane) and shear stress distribution along the cross section (in the $y$-$z$ plane): (a) $100 \leqslant \mathrm{Re}_{D_h} \leqslant 438$, (b) $438 < \mathrm{Re}_{D_h} \leqslant 758$, and (c) $\mathrm{Re}_{D_h} > 758$.

## IV. CONCLUSIONS

To stipulate fluidic mechanisms responsible for the reversal of flow resistance caused by low Reynolds number laminar flow in both reference and cavitied microchannels, a series of pressure and flow field measurements are conducted. The main conclusions are summarized as follows.

(a) The reversal of flow resistance by laminar flow in a microchannel occurs due to geometric modifications such as cavities.

(b) At very low Reynolds numbers, the stagnant fluid inside cavities acts as a buffer layer between the mainstream and the cavity's concave sidewalls. Flow slippage along the interface between mainstream and stagnant fluid in the cavity results in a lower flow resistance in the cavitied microchannels compared to the reference microchannels. The decrease in flow resistance is the same regardless of whether two-dimensional or three-dimensional cavities are used.

(c) Increasing Reynolds number initiates the circulation of irrotational vortices in the cavity, causing a slight yet continuous increase in wall shear stresses along concave cavity surfaces. Meanwhile, the unstable boundary layers are generated along the cavity interface.

(d) The flow resistance in the cavitied microchannels eventually becomes equivalent to that of the reference (unmodified) microchannels as the Reynolds number is increased further, reaching the reversal Reynolds number.

(e) As the Reynolds number is further increased, vortices in cavities are enlarged and become rotational. Thus, these vortices substantially increase wall shear stresses along concave cavity surfaces. Meanwhile, the circulating rotational flow intensifies instabilities along the cavity interface.

(f) Further, the intensified instabilities trigger the earlier transition of laminar flow to turbulent flow, i.e., at a lower (critical) Reynolds number.

(g) The increased surface area offered by three-dimensional cavities is predicated to have amplified the increase in wall shear stresses and resulted in an earlier onset in flow resistance reversal—having a lower critical and reversal Reynolds number.

The data that support the findings of this study are available within the article.

## ACKNOWLEDGMENTS

This work was supported by the Open Fund of the National Key Laboratory of Mechanics and Control for Aerospace Structures (MCMS-E-0219 K02), the Double Innovation Talent Foundation of Jiangsu Province (JSSCRC2021502), and the National Natural Science Foundation of China (Grant No. 12032010).

T.K. conceived the idea. T.J.L. secured funding for the project. Y.Y.L. designed the experiments and performed the *in situ* measurements. M.X.L. guided the use of $\mu$PIV. Y.Y.L., S.W.S., and T.K. performed the data analysis. Y.Y.L., S.W.S., and T.K. wrote the manuscript. M.X.L., T.J.L., and T.K. revised the manuscript.

The authors declare no competing interests.

[1] G. M. Whitesides, The origins and the future of microfluidics, Nature (London) **442**, 368 (2006).

[2] S. G. Kandlikar, S. Garimella, D. Li, S. Colin, and M. R. King, *Heat Transfer and Fluid Flow in Minichannels and Microchannels*, 2nd ed. (Butterworth-Heinemann, Oxford, UK, 2014), pp. 1–9.

[3] J. Zhang, S. Yan, R. Sluyter, W. Li, G. Alici, and N.-T. Nguyen, Inertial particle separation by differential equilibrium positions in a symmetrical serpentine micro-channel, Sci. Rep. **4**, 4527 (2014).

[4] S. O. Hong, K.-S. Park, D.-Y. Kim, S. S. Lee, C.-S. Lee, and J. M. Kim, Gear-shaped micromixer for synthesis of silica particles utilizing inertio-elastic flow instability, Lab Chip **21**, 513 (2021).

[5] F. Bartels, S. Dahms, U. Kampmeyer, and M. Rawert, Method for supplying a fluid and micropump for said purpose, US Patent No. 20110005606A1 (2011).

[6] W. W. Wits, S. J. Weitkamp, and J. van Es, Metal additive manufacturing of a high-pressure micro-pump, Procedia CIRP **7**, 252 (2013).

[7] R. van Erp, G. Kampitsis, and E. Matioli, Efficient microchannel cooling of multiple power devices with compact flow distribution for high power-density converters, IEEE Trans. Power Electron. **35**, 7235 (2020).

[8] B. R. Munson, T. H. Okiishi, W. W. Huebsch, and A. P. Rothmayer, *Fundamentals of Fluid Mechanics*, 7th ed. (Wiley, New York, 2012), pp. 426–431.

[9] G. Xia, L. Chai, M. Zhou, and H. Wang, Effects of structural parameters on fluid flow and heat transfer in a microchannel with aligned fan-shaped reentrant cavities, Int. J. Therm. Sci. **50**, 411 (2011).

[10] L. Chai, G. Xia, M. Zhou, and J. Li, Numerical simulation of fluid flow and heat transfer in a microchannel heat sink with offset fan-shaped reentrant cavities in sidewall, Int. Commun. Heat Mass Transfer **38**, 577 (2011).

[11] H. Li, Y. Li, B. Huang, and T. Xu, Numerical investigation on the optimum thermal design of the shape and geometric parameters of microchannel heat exchangers with cavities, Micromachines **11**, 721 (2020).

[12] Z. He, Y. Yan, and Z. Zhang, Thermal management and temperature uniformity enhancement of electronic devices by micro heat sinks: A review, Energy **216**, 119223 (2021).

[13] See Supplemental Material at http://link.aps.org/supplemental/10.1103/PhysRevFluids.9.044201 for time-averaged flow field measurements using micro-particle image velocimetry.
[14] M. Raffel, C. E. Willert, F. Scarano, C. J. Kähler, S. T. Wereley, and J. Kompenhans, *Particle Image Velocimetry: A Practical Guide*, 3rd ed. (Springer, New York, 2018), pp. 367–412.
[15] R. J. Adrian and J. Westerweel, *Particle Image Velocimetry* (Cambridge University Press, Cambridge, 2011), pp. 205–217.
[16] M. G. Olsen and R. J. Adrian, Out-of-focus effects on particle image visibility and correlation in microscopic particle image velocimetry, Exp. Fluids **29**, S166 (2000).
[17] C. D. Meinhart, S. T. Wereley, and M. H. B. Gray, Volume illumination for two-dimensional particle image velocimetry, Meas. Sci. Technol. **11**, 809 (2000).
[18] See Supplemental Material at http://link.aps.org/supplemental/10.1103/PhysRevFluids.9.044201 for uncertainty analysis.
[19] H. W. Coleman and W. G. Steele, *Experimentation, Validation, and Uncertainty Analysis for Engineers*, 3rd ed. (Wiley, New York, 2018).
[20] J. G. Santiago, S. T. Wereley, C. D. Meinhart, D. J. Beebe, and R. J. Adrian, A particle image velocimetry system for microfluidics, Exp. Fluids **25**, 316 (1998).
[21] A. K. Prasad, R. J. Adrian, C. C. Landreth, and P. W. Offutt, Effect of resolution on the speed and accuracy of particle image velocimetry interrogation, Exp. Fluids **13**, 105 (1992).
[22] J. Westerweel, On velocity gradients in PIV interrogation, Exp. Fluids **44**, 831 (2008).
[23] J. Westerweel, Theoretical analysis of the measurement precision in particle image velocimetry, Exp. Fluids **29**, S003 (2000).
[24] J. C. F. Pereira and J. M. M. Sousa, Experimental and numerical investigation of flow oscillations in a rectangular cavity, J. Fluids Eng. **117**, 68 (1995).
[25] H. Yao, R. K. Cooper, and S. Raghunathan, Numerical simulation of incompressible laminar flow over three-dimensional rectangular cavities, J. Fluids Eng. **126**, 919 (2004).
[26] R. K. Shah and A. L. London, Laminar flow forced convection in ducts, *A Source Book for Compact Heat Exchanger Analytical Data* (Academic, New York, 1978), pp. 253–279.